J. Fluid Mech. (2014), *vol.* 748, *pp.* 768–788. © Cambridge University Press 2014
doi:10.1017/jfm.2014.217

Conditions for extreme wave runup on a vertical barrier by nonlinear dispersion

Claudio Viotti[1,†], Francesco Carbone[1] and Frédéric Dias[1,2]

[1]School of Mathematical Sciences, University College of Dublin, Ireland

[2]CMLA, ENS Cachan, 61 avenue du Président Wilson, 94235 Cachan CEDEX, France

(Received 28 October 2013; revised 4 March 2014; accepted 14 April 2014;
first published online 8 May 2014)

The runup of long strongly nonlinear waves impinging on a vertical wall can exceed six times the far-field amplitude of the incoming waves. This outcome stems from a precursory evolution process in which the wave height undergoes strong amplification due to the combined action of nonlinear steepening and dispersion, resulting in the formation of nonlinearly dispersive wave trains, i.e. undular bores. This part of the problem is first analysed separately, with emphasis on the wave amplitude growth rate during the development of undular bores within an evolving large-scale background. The growth of the largest wave in the group is seen to reflect the asymptotic time scaling provided by nonlinear modulation theory rather closely, even in the case of fully nonlinear evolution and moderately slow modulations. In order to address the effect of such a dynamics on the subsequent wall runup, numerical simulations of evolving long-wave groups are then carried out in a computational wave tank delimited by vertical walls. Conditions for optimal runup efficiency are sought with respect to the main physical parameters characterizing the incident waves, namely the wavelength, the length of the propagation path and the initial amplitude. Extreme runup is found to be strongly correlated to the ratio between the available propagation time and the shallow-water nonlinear time scale. The problem is studied in the twofold mathematical framework of the fully nonlinear free-surface Euler equations and the strongly nonlinear Serre–Green–Naghdi model. The performance of the reduced model in providing accurate long-time predictions can therefore be assessed.

Key words: geophysical and geological flows, ocean processes, shallow water flows

1. Introduction

The wave runup on a vertical wall is a problem of both fundamental and practical interest. For instance, the proper design of most coastal structures (i.e. sea walls, breakwaters, etc.) relies on accurate estimation of various dynamical wave–wall interactions, including wave runup. In engineering, it is common practice to rely on the notion of a design wave for the estimation of the critical conditions that must be accounted for in the course of structure design (see, e.g. Sainflou 1928; Goda 2010). It is by no means a simple task, however, to predict the maximum wave

† Email address for correspondence: claudio.viotti@ucd.ie

https://doi.org/10.1017/jfm.2014.217 Published online by Cambridge University Press

amplitude that a coastal structure can experience in a given sea state, or during unforeseen events, and therefore to determine which conditions can suggest effective design-wave prototypes. In a recent publication, Carbone *et al.* (2013) have shown that an apparently simple set-up, consisting of an initially near-monochromatic wave group approaching a vertical barrier over flat bathymetry, can produce remarkably strong runups (about six times the initial amplitude of the incoming wave) by the combined action of nonlinear and dispersive dynamics. This result emphasized the need to account for such counterintuitive scenarios in defining an effective notion of a design wave.

Following the work of Carbone *et al.* (2013), we focus on the evolution of long waves over flat bathymetry. Recent natural events, such as the 2004 tsunami in the Indian Ocean and the 2011 tsunami in Japan, have steered new interest towards the study of long oceanic waves, e.g. tsunamis and landslide-generated waves, and their potentially hazardous effects over populated coasts. In this context, the wave runup over sloping shores, i.e. the inland penetration of highly destructive floods, has received most attention (e.g. Fritz *et al.* 2007; Madsen & Schäffer 2010; Fritz *et al.* 2011; Mori *et al.* 2011; Fritz *et al.* 2012). Even though the vertical runup associated with long waves has attracted less interest, it is now recognized that the long-time evolution of long oceanic waves can spawn unexpectedly large vertical amplifications (Grue *et al.* 2008; Tissier *et al.* 2011; Zhao, Liu & Wang 2013). The interplay between nonlinear wave steepening and dispersion eventually leads the wave dynamics, provided that enough propagation time is available. As a result, a system of elevations and depressions of the sea surface evolves by nonlinear steepening from the shallow-water regime into undular bores characterized by strong rapid oscillations, which ultimately disintegrate into an expanding train of solitary waves. Grue *et al.* (2008) provided evidence that such a process, characterized by strongly nonlinear and dispersive dynamics neglected in the traditional dispersionless shallow-water framework, occurred during the propagation of tsunami waves in specific regions of the continental shelf. In general, it is now recognized that both nonlinearity (Pelinovsky *et al.* 1999; Antuono & Brocchini 2007) and dispersion are crucial for the correct modelling of long-wave dynamics and the associated runup (Grue *et al.* 2008; Tissier *et al.* 2011).

The recent study by Carbone *et al.* (2013), which investigated the vertical runup ensuing from the above dynamics in terms of the overall amplification factor with respect to the initial amplitude of the generated waves, suggests that extreme runup, greatly exceeding predictions based on dispersionless theories (Pelinovsky *et al.* 1999), requires full disintegration of the initial long waves into a train of solitary-like waves prior to the wave–wall interaction. For the case of a single solitary wave, the vertical runup (equivalent, when neglecting viscosity, to a symmetric head-on collision) has been examined by several authors, who have elucidated several characteristics of nonlinear runup, namely nonlinearly enhanced runup (e.g. Su & Mirie 1980; Craig *et al.* 2006), post-collision phaseshift (e.g. Maxworthy 1976; Su & Mirie 1980), trailing-wave formation (e.g. Byatt-Smith 1988; Craig *et al.* 2006), wall residence time (e.g. Temperville 1979; Cooker, Weidman & Bale 1997; Chambarel, Kharif & Touboul 2009) and residual jet formation (Chambarel *et al.* 2009), for very large wave amplitudes (above 0.6 times the water depth). In contrast to previous runup studies, the aim of the present paper is to characterize the evolution from the shallow-water to the dispersive regime described above in relation to the establishment of near-wall conditions favourable to extreme vertical runup. In particular, we investigate the conditions that lead to wall runup enhancements, the temporal and spatial scales on

https://doi.org/10.1017/jfm.2014.217 Published online by Cambridge University Press

which such conditions emerge and how these are related to the characteristics of the initial waves (wavelength, propagation length and initial amplitude).

As different regimes occur during the whole time evolution, we further emphasize the need to rely on a mathematical model that is able to capture dispersion and nonlinearity at a sufficient level of refinement. Therefore, this paper also constitutes an attempt to address the role of mathematical modelling. In particular, we intend to assess the performance of the Serre–Green–Naghdi (SGN) system (Serre 1953; Green, Laws & Naghdi 1974; Green & Naghdi 1976; Zheleznyak & Pelinovsky 1985) in comparison with the full Euler equations. The SGN system has proved successful in the study of large-amplitude and even near-breaking waves in the nearshore. In particular, the accuracy of the SGN system in describing strongly nonlinear shallow water waves has been confirmed by comparisons between numerical simulations and experiments on solitary waves over variable topography, e.g. Temperville, Seabra-Santos & Renouard (1987), and wave shoaling and breaking over beach slopes, see Barthélemy (2004), Cienfuegos, Barthélemy & Bonneton (2007) and Cienfuegos, Barthélemy & Bonneton (2010). However, very few studies have been performed on the propagation of long wave groups and on the runup phenomena for wave groups and their subsequent interaction with rigid structures in the nearshore zone. We also mention the hyperbolic model derived by Antuono, Liapidevskii & Brocchini (2009), referred to as dispersive nonlinear shallow-water equations (DNSWEs), as an alternative to the SGN system. Even though we will not consider such a model in the present study, we observe that it has dispersive and strongly nonlinear properties which make it appealing for use in analogous contexts.

We further remark that the subject of this work can have a connection to the freak wave phenomenon in the shallow-water regime, where we recall in this context that over 80 % of reported past freak wave events have been in shallow waters or coastal areas, as reported by Nikolkina & Didenkulova (2011) and O'Brien, Dudley & Dias (2013). Even though this high percentage is likely to be biased by the fact that there are more observations near the shore than offshore, there is no doubt that freak waves also occur in shallow water.

This paper is organized as follows. In § 2 we present the formulation of the problem and the governing equations. The numerical approach and set-up are described in § 3. Results are reported in § 4, which is divided into four parts: § 4.1 contains an in-depth discussion of the development of undular bores within inhomogeneous backgrounds, and in §§ 4.2–4.4 we address the dependence of the runup on the spatial scale, propagation length and nonlinearity respectively. Conclusions are summarized in § 5.

2. Governing equations

We consider a two-dimensional wave tank with a flat impermeable bottom of uniform depth d and length $2L$, filled with an incompressible inviscid fluid. The (x, y) coordinate system is chosen with the vertical upward pointing y-axis, along which acts the acceleration due to gravity g, and the horizontal x-axis coinciding with the undisturbed water level $y = 0$. The two evolution models considered, i.e. the fully nonlinear Euler equations and the SGN model, are outlined in what follows. All variables are understood to be dimensional (in SI units). Whenever results are expressed in terms of non-dimensional groups, the physical dimensional magnitudes can be obtained by referring to a typical depth $d = 10$–50 m and $g = 9.8$ m s^{-2}.

https://doi.org/10.1017/jfm.2014.217 Published online by Cambridge University Press

2.1. *Free-surface Euler equations*

By assuming inviscid irrotational flow inside the fluid volume, the free-surface dynamics is governed by the free-surface Euler system

$$\eta_t = -\phi_x\eta_x + \phi_y, \quad \text{at } y = \eta(x, t), \tag{2.1}$$

$$\phi_t = -\tfrac{1}{2}\left(\phi_x{}^2 + \phi_y{}^2\right) - g\eta, \quad \text{at } y = \eta(x, t), \tag{2.2}$$

$$\nabla^2\phi = 0, \quad \text{for } -d < y < \eta(x, t), \ 0 < x < 2L, \tag{2.3}$$

subject to the boundary conditions

$$\phi_y = 0, \quad \text{at } y = -d, \tag{2.4}$$

$$\phi_x = 0, \quad \text{at } x = 0, 2L. \tag{2.5}$$

In the above equations $\eta(x, t)$ is the free surface elevation with respect to the unperturbed condition and $\phi(x, y, t)$ is the velocity potential. The boundary conditions (2.4) and (2.5) express the usual slip-wall condition on the bottom of the tank and on the side vertical walls respectively. Surface tension effects are negligible for the characteristic spatial scales of interest in this study.

The crucial challenge presented by the water wave problem consists of obtaining the fluid velocity at the free surface from the knowledge of the wave profile, η, and the potential at the free surface, $\overline{\phi}(x, t) \equiv \phi(x, \eta(x, t), t)$. These quantities are coupled through the Laplace equation for ϕ within the time-dependent fluid domain. In a two-dimensional flow this problem can be conveniently handled by the conformal-mapping approach, which consists of mapping the free-surface system (2.1)–(2.3) into an equivalent problem formulated in the conformal (ξ, ζ) space inside the uniform strip $0 < \xi < 2L$, $-\overline{d} < \zeta < 0$. Such a mapping is expressed through the analytic coordinate transformation

$$Z = X(\xi, \zeta, t) + \mathrm{i}Y(\xi, \zeta, t) \tag{2.6}$$

and the complex potential

$$\Phi(\xi, \zeta, t) + \mathrm{i}\Psi(\xi, \zeta, t) = \phi(X, Y) + \mathrm{i}\psi(X, Y), \tag{2.7}$$

where capitals are used for those variables regarded as functions of the conformal coordinates (ξ, ζ). In the conformal space, standard results of complex analysis allow one to relate harmonic-conjugate variables, i.e. (X, Y) and (Φ, Ψ), in terms of Hilbert-transform-like operators, and to reconstruct all the necessary quantities by working only on the free surface ($\zeta = 0$). In particular, on the free surface we have that

$$X_\xi = 1 - \mathscr{T}_c[Y_\xi], \quad \Psi_\xi = -\mathscr{T}_s[\Phi_\xi], \tag{2.8a,b}$$

where

$$\mathscr{T}_c[f] = \frac{1}{2\overline{d}} \fint f(\xi') \coth[\pi(\xi' - \xi)/2\overline{d}]\mathrm{d}\xi', \tag{2.9}$$

$$\mathscr{T}_s[f] = -\frac{1}{2\overline{d}} \fint f(\xi')\mathrm{cosech}[\pi(\xi' - \xi)/2\overline{d}]\mathrm{d}\xi'. \tag{2.10}$$

https://doi.org/10.1017/jfm.2014.217 Published online by Cambridge University Press

After some manipulations, which we omit for the sake of conciseness (details can be found, e.g. in Choi & Camassa (1999) or Li, Hyman & Choi (2004)), equations (2.1) and (2.2) become

$$Y_t = -X_\xi \left(\frac{\Psi_\xi}{J}\right) + Y_\xi \mathscr{T}_c\left[\frac{\Psi_\xi}{J}\right] + Y_\xi q(t), \tag{2.11}$$

$$\Phi_t = -\frac{1}{J}\left[\frac{1}{2}\Phi_\xi^2 - \frac{1}{2}\Psi_\xi^2 - J\Phi_\xi \mathscr{T}_c(\Psi_\xi/J)\right] - gY + C(t), \tag{2.12}$$

where $J = X_\xi^2 + Y_\xi^2$. The above system, together with the constitutive relations (2.8), represents a closed dynamical system which is suitable for direct numerical discretization (outlined in § 3).

2.2. *The Serre–Green–Naghdi strongly nonlinear model*

In the long-wave regime, the dynamics of strongly nonlinear dispersive shallow-water waves is asymptotically approximated by the solution of the SGN equations. The SGN system is a classic model derived from the full Euler system (2.1)–(2.3) by assuming that the characteristic horizontal wavelength, λ, is large compared with the vertical scale d, i.e. by carrying out an asymptotic expansion in the small parameter $\epsilon = d/\lambda \ll 1$ and retaining terms up to $\mathcal{O}(\epsilon^3)$. No assumption is made on the magnitude of the vertical displacements; hence the SGN system is regarded as a strongly nonlinear and weakly dispersive model (Lannes & Bonneton 2009; Dias & Milewski 2010). The SGN system improves the basic shallow-water theory by including dispersive effects contained in the third-order terms. In dimensional form the SGN system can be cast as

$$h_t + (h\tilde{u})_x = 0, \tag{2.13}$$

$$\tilde{u}_t + \left(\tfrac{1}{2}\tilde{u}^2 + gh\right)_x = \tfrac{1}{3}h^{-1}\left[h^3\left(\tilde{u}_{xt} + \tilde{u}\tilde{u}_{xx} - \tilde{u}_x^2\right)\right]_x, \tag{2.14}$$

where $h(x, t) = \eta(x, t) + d$ is the total water depth and $\tilde{u}(x, t)$ is the depth-averaged horizontal velocity. The right-hand side of (2.14) contains the terms that account for non-hydrostatic and dispersive effects. It should be noted that such an equation constitutes an implicit evolution equation for $\tilde{u}$, since a time derivative appears also on the right-hand side. For the numerical solution of the SGN system, it is therefore convenient to introduce the auxiliary variable

$$q = \tilde{u} - \tfrac{1}{3}h^2\tilde{u}_{xx} - hh_x\tilde{u}_x, \tag{2.15}$$

which allows one to rewrite (2.14) in the explicit evolutive form

$$q_t = \left[\tfrac{1}{2}\tilde{u}^2 + \tfrac{1}{2}h^2\tilde{u}_x^2 - g(h-d) - q\tilde{u}\right]_x. \tag{2.16}$$

3. Numerical methodology and set-up

Both evolution systems considered are discretized in space using a spectral method. For the Euler equations, the Fourier spectral expansion is applied directly to the conformal-space formulation given by (2.11) and (2.12),

$$\eta(\xi, t) = \sum_{n=-N/2}^{N/2} \hat{\eta}_n(t)\mathrm{e}^{\mathrm{i}n\kappa\xi}, \quad \phi(\xi, t) = \sum_{n=-N/2}^{N/2} \hat{\phi}_n(t)\mathrm{e}^{\mathrm{i}n\kappa\xi}, \tag{3.1a,b}$$

https://doi.org/10.1017/jfm.2014.217 Published online by Cambridge University Press

where $\kappa = \pi/L$. The conversion from physical to conformal space and vice versa is carried out in pre- and postprocessing. Likewise, for the SGN variables we have

$$h(x,t) = \sum_{n=-N/2}^{N/2} \hat{h}_n(t)\mathrm{e}^{\mathrm{i}n\kappa x}, \quad q(x,t) = \sum_{n=-N/2}^{N/2} \hat{q}_n(t)\mathrm{e}^{\mathrm{i}n\kappa x}. \tag{3.2a,b}$$

The nonlinear right-hand sides of both systems are assembled through a classic pseudo-spectral procedure. The governing equations are then transformed in Fourier space with the classic pseudo-spectral treatment of the nonlinear terms performed via fast Fourier transform (FFT). Aliasing errors due to the nonlinear interaction between Fourier modes, and affecting high wavenumbers, can be removed in different ways. Li *et al.* (2004), for instance, use a small artificial viscosity to damp the 1/2 higher wavenumbers. Here, on the contrary, we prefer a zero-padding approach (Patterson & Orszag 1971) based on the 1/2-rule, consisting of a complete filtering of the 1/2 higher wavenumbers after any nonlinear operation is performed (hence it is somewhat stronger than the standard 1/3-rule used for quadratic nonlinearities). Even though in the case of fully nonlinear water waves no method can completely remove aliasing errors due to the infinite-order nonlinearity, this method proved satisfactory.

We remark that numerical solution of the SGN system (2.13) and (2.16) requires one to solve (2.15) in order to update the primitive variable $\tilde{u}$ before any evaluation of the right-hand side. This is carried out here by fixed-point iterations, as described by Dutykh *et al.* (2013). For time marching we employ a high-order multistep method in the case of the Euler system and a high-order Runge–Kutta routine for the SGN system. The typical numerical resolution that we employ ranges from $N = 8192$ to $N = 32\,768$ dealiased Fourier modes, tuned according to the ratio between the smallest scales to be resolved and the domain size. In doing so, we represent the shortest waves with a number of collocation points (typically $\approx$100) sufficient to fully resolve sharp wave crests, especially during runup events. This resolution ensures a relative error in the total energy conservation of no more than 10^{-8} at the final simulation time.

In the work of Carbone *et al.* (2013), which was limited to the framework of the SGN equations, the problem was approached numerically by a finite-volume scheme, suitable for the implementation of a wavemaker and rigid-wall boundary conditions. Since the spectral discretization is only compatible with periodic boundary conditions we need to rely on a different strategy in order to realize the effect of a vertical wall. To this end, we follow a classic reflection method, already applied, for instance, by Zabusky & Kruskal (1965), Bona, Pritchard & Scott (1980), Fenton & Rienecker (1982) and Craig *et al.* (2006), which can be used in the absence of viscosity. That is, we impose mirror symmetry about the centreline $x = L$ of the computational domain in the initial condition, which remains preserved at any time due to the complete symmetry of the problem. This ensures a constant null horizontal velocity at $x = L$, equivalent to the presence of a rigid vertical wall. The effective physical domain is therefore $0 < x < L$, which is bounded on the right-hand side by a vertical wall. This set-up is illustrated in figure 1. We remark that the effective equivalence between vertical-wall reflection and symmetric head-on collision in the absence of viscosity seems to be a safe assumption even when a small viscosity is present, at least for a Reynolds number typical for oceanic waves. In this regard, we mention the results by Camfield & Street (1968), as reported by Chan & Street (1970), which to the best of our knowledge represent the only experimental results available.

3.1. *Initialization*

We employ an initial condition consisting of a simple linear wave, $a_0 \sin(k_0 x - \omega_0 t)$, multiplied by an envelope function, $W(x)$. The linear dispersion relation differs for the

https://doi.org/10.1017/jfm.2014.217 Published online by Cambridge University Press

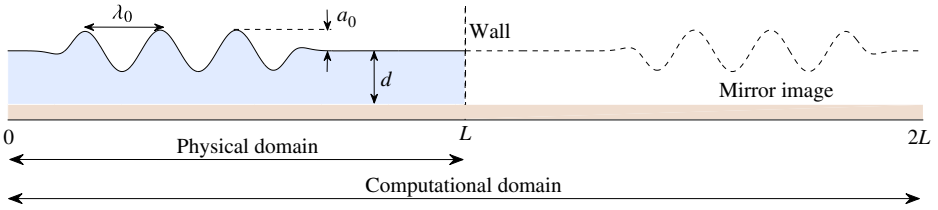


FIGURE 1. (Colour online) Schematic of the physical and computational set-ups. The wave profile represents the initial condition (proportions are altered for clarity).

two systems. Namely, for the Euler system we have the finite-depth linear dispersion relation

$$\omega_0^2 = gk_0 \tanh(dk_0), \tag{3.3}$$

whereas the SGN system possesses the (weakly) dispersive relation

$$\omega_0^2 = gdk_0^2/\left(1 + \tfrac{1}{3}d^2k_0^2\right). \tag{3.4}$$

We then proceed by matching the time frequency ω_0 between the Euler and SGN initial conditions. The values of the initial wavelength that we consider span a wide range, but the condition $\lambda_0 \gg d$ is always satisfied ($10^{-3} < O(\lambda_0/d) < 10^{-1}$), whereby we also obtain a close match of the initial wavelength $\lambda_0 = 2\pi/k_0$ between the two evolution systems.

For the Euler equations, the initial condition is assigned in terms of the surface displacement, $\eta(x, t)$, and velocity potential at the free surface, $\overline{\phi}(x, t)$,

$$\eta_0(x) = W(x)a_0 \sin k_0(x - x_0), \tag{3.5}$$

$$\overline{\phi}_0(x) = -W(x)a_0 \frac{\omega_0}{k_0} \coth dk_0 \cos k_0(x - x_0), \tag{3.6}$$

whereas for the SGN system it is assigned in terms of η and $\tilde{u}$,

$$\eta_0(x) = W(x)a_0 \sin k_0(x - x_0), \tag{3.7}$$

$$\tilde{u}_0(x) = W(x)a_0 \frac{\omega_0}{dk_0} \sin k_0(x - x_0). \tag{3.8}$$

The objectivity of the linear wave solution provides a natural equivalence between the initializations of the two models, despite the fact that these are based on different variables. The main physical parameters that characterize the initial condition are therefore the linear time frequency ω_0, the amplitude a_0 and the distance from the wall. The initial distance between the wave group and the wall determines the available evolution time the wave group has prior to the wall interaction. The envelope function is defined as

$$W(x) = \frac{1}{2}\tanh\left(\frac{x - x_0}{\delta}\right) - \frac{1}{2}\tanh\left(\frac{x - x_0 - N_w\lambda_0}{\delta}\right), \tag{3.9}$$

which produces a wavepacket containing N_w full wavelengths (figure 1).

The effect of the number of waves contained in a wave group on the ensuing runup was addressed by Carbone *et al.* (2013). They found that the runup efficiency increases

https://doi.org/10.1017/jfm.2014.217 Published online by Cambridge University Press

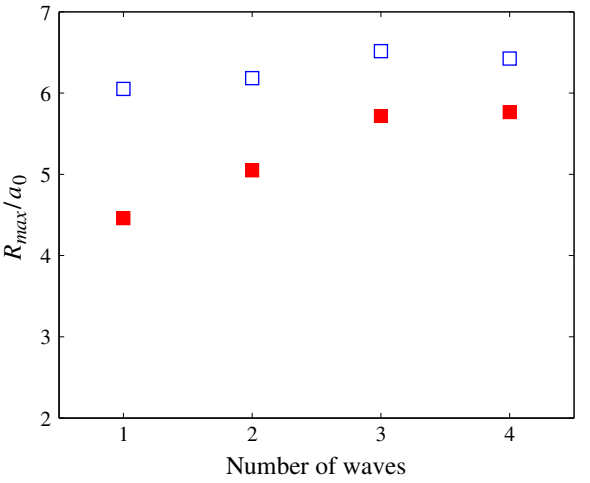


FIGURE 2. (Colour online) Maximum normalized runup, as defined in (4.2), as a function of the number of waves, N_w, in the initial wave group, for $\lambda_0 = 125d$ (filled squares) and $\lambda_0 = 250d$ (empty squares). The distance from the centre of the wave group to the wall at $t = 0$ is maintained constant and equal to $15/4\lambda_0$ (which amounts to $L = 6\lambda_0$ for $N_w = 3$).

substantially from the case $N_w = 1$ to $N_w = 3$, and remains essentially constant beyond this point. In figure 2 we confirm that this trend still holds for the present set-up. Accordingly, we focus on the critical $N_w = 3$ case from now on.

The value of the thickness parameter, δ, in (3.9) affects the wave evolution at startup. While the carrier wave is purely progressive by construction, the same property is not guaranteed to hold for all wavenumbers after the envelope function is applied. As a consequence, secondary counterpropagating waves form near the flanks of the wave group. Figure 3 illustrates this behaviour, as the oscillatory character of the Fourier coefficients denotes the presence of counterpropagating waves. This plot also shows how larger values of δ, i.e. milder envelopes, can be employed in order to alleviate this effect. Since overlarge values of δ, on the other hand, present the downside of smoothing the leading wavefront, we opted for the choice $\delta \approx 0.2\lambda_0$ as a satisfactory compromise which yields wave groups analogous to the ones generated by boundary forcing by Carbone *et al.* (2013). We further stress that, in any case, the long-time evolution (and the ensuing runup) is found to be robust with respect to the formation of spurious waves, since these disentangle from the main wave group leaving behind no noticeable effects. The initial offset of the wave group from the left-hand boundary, x_0, raises a similar concern. By taking x_0 as $3\lambda_0/4$, cut-off effects are completely negligible.

4. Results

Our goal is to study the effect of different physical parameters on the wall runup and to elucidate the underlying physics. We define the wave runup as the free surface elevation at the wall (located at $x = L$), i.e.

$$R(t) = \eta(L, t), \tag{4.1}$$

and the maximum runup over an entire time record as

$$R_{max} = \max_t [R(t)]. \tag{4.2}$$

https://doi.org/10.1017/jfm.2014.217 Published online by Cambridge University Press

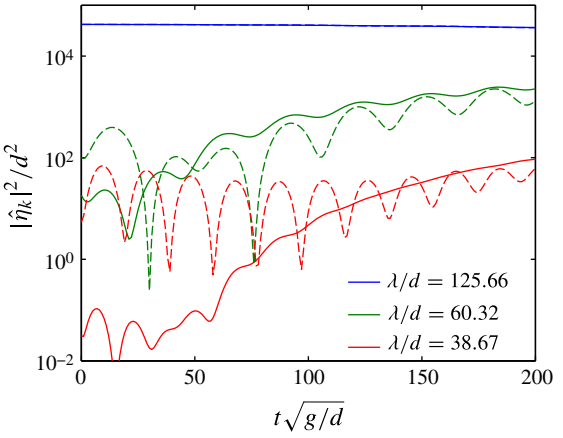


FIGURE 3. (Colour online) The time evolution of the squared magnitude of three Fourier coefficients of the free surface elevation during the early transient from Euler numerical simulation. Solid lines correspond to $\delta = 0.28\lambda_0$ and dashed lines to $\delta = 0.12\lambda_0$. The parameters used in this example are $\lambda_0 = 125d$ ($\omega_0 = 0.05\sqrt{g/d}$) and $a_0 = 0.05d$.

The typical time evolution observed in our numerical experiments is illustrated in figure 4, and can be summarized in a sequence of different stages. The first stage is governed by shallow-water dynamics. As such, the wave profile undergoes nonlinear steepening and develops sharp fronts on the leading front of the waves. This process eventually triggers higher-order dispersive effects, which characterize a second stage. Here, rapid oscillations develop, which regularize the steep fronts into undular bores, and can be viewed as modulated cnoidal waves evolving under the influence of nonlinear dispersion (Whitham 1974; El, Grimshaw & Smyth 2006; Tissier *et al.* 2011). This second process is characterized by strong wave amplification: the maximum wave amplitude amounts to a growth factor of approximately 2–2.5 of the initial amplitude a_0, depending on λ_0 and a_0. Since the growth rate of the fast undulations plays an important role in determining the subsequent wave runup, we first carry out an in-depth discussion of this process in § 4.1. A third stage takes place as the waves reach the wall, where runup occurs together with reflection. This part will be examined in §§ 4.2–4.4. The whole process is visualized in figure 4, where the typical wave pattern can be observed.

4.1. *Time scaling of wave amplification in developing undular bores*

The wave growth due to the formation of undular bores (also referred to as dispersive shocks) strongly affects the subsequent wave runup. This problem has been studied since the seminal work of Peregrine (1966), for the classic case of a wavefront separating two homogeneous currents. As already observed by Peregrine (1966) and, more recently, by Wei *et al.* (1995), the growth of the fast undulations is not amenable to close theoretical prediction, and furthermore it depends to a large extent on the specific initial conditions. We further stress that, in contrast to the case discussed in the above papers, here we are in the presence of an unsteady inhomogeneous background.

The notions of background flow and fast oscillations can be made precise in the context of Whitham's modulation theory (Whitham 1974). Referring for definitiveness

https://doi.org/10.1017/jfm.2014.217 Published online by Cambridge University Press

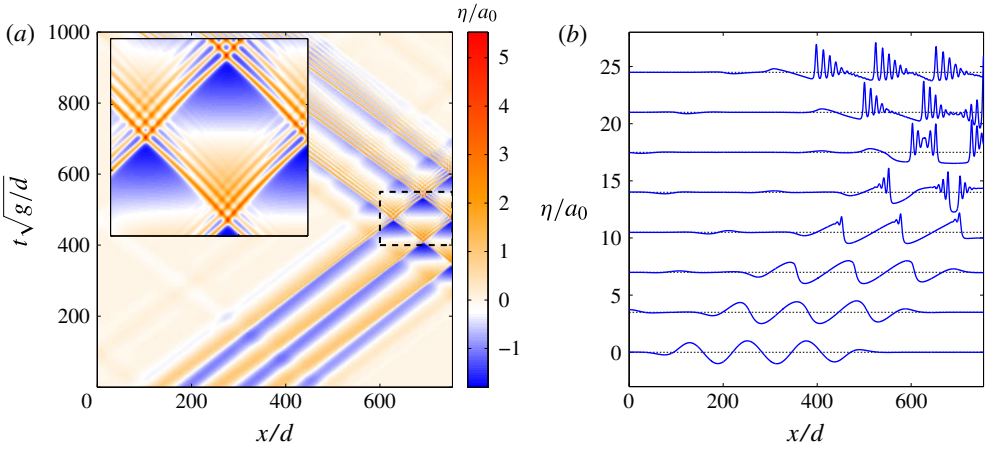


FIGURE 4. (Colour online) Typical space–time evolution of the normalized free-surface elevation considered in this study, in which a wavepacket approaches and subsequently impinges on the vertical wall located at the right boundary of the domain. The colourmap (*a*) and line plots (*b*) show the same numerical solution of the free-surface Euler equations, with parameters $\omega_0 = 0.05\sqrt{g/d}$ and $a_0 = 0.05d$. The inset in the colourmap is a blowup of the near-wall area enclosed in the dashed rectangle. The surface elevation plots in (*b*) are taken from $t = 0$ with $\Delta t = 100\sqrt{d/g}$ intervals (time increases upward and curves are progressively upshifted).

to the SGN equations (2.13) and (2.14), the solution is written as a periodic nonlinear travelling wave (i.e. a cnoidal wave)

$$\eta = N(\theta; \overline{\eta}, \overline{u}, \kappa, \alpha), \quad \tilde{u} = U(\theta; \overline{\eta}, \overline{u}, \kappa, \alpha), \quad \theta = \kappa x - \Omega t, \tag{4.3a,b}$$

parameterized by the slowly varying (in both space and time) wavenumber κ, amplitude α, and the local depth and velocity $\overline{\eta} = \int_0^{2\pi} \eta \mathrm{d}\theta$ and $\overline{u} = \int_0^{2\pi} u \mathrm{d}\theta$, defined by local period averaging. The frequency $\Omega(\kappa, \alpha)$ represents the nonlinear dispersion relation. Whitham's averaged conservation law formalism yields the nonlinear modulation equations, an evolutive system for $\overline{\eta}$, $\overline{u}$, κ, α, where $\overline{\eta}$ and $\overline{u}$ represent the slow background, while κ and α characterize the rapid (but slowly modulated) oscillations. El *et al.* (2006) have applied this method to the SGN equations for the study of undular bores developing from an initial step front between subcritical and supercritical plane currents. Even though we do not intend to enter into the details of the theory, it is useful to adopt some of its elements as guidelines. The method can be cast as a multiscale expansion, in which both the background and the modulation are assumed to evolve on slow spatial and temporal scales. In the absence of fast oscillations ($\alpha = 0$, $\eta = \overline{\eta}$, $\tilde{u} = \overline{u}$), the modulation equations reduce to the dispersionless nonlinear shallow-water equations for the background variables (El *et al.* 2006),

$$\overline{\eta}_t + \overline{u}\,\overline{\eta}_x + (\overline{\eta} + d)\overline{u}_x = 0, \tag{4.4}$$

$$\overline{u}_t + \overline{u}\,\overline{u}_x + g\overline{\eta}_x = 0, \tag{4.5}$$

which govern the dynamics until wave steepening triggers high-order dispersive effects.

Since here we are focusing on the stage prior to the wave–wall interaction, we consider the case of a one-directional plane wave over a flat bottom, characterized

https://doi.org/10.1017/jfm.2014.217 Published online by Cambridge University Press

by wavelength λ_0, frequency ω_0 and amplitude a_0, as in (3.5). The evolution of this preliminary case reproduces the same bore formation process as described in the previous section and visualized in figure 4, but can be followed up to an indefinitely long time due to the absence of physical boundaries. During early time evolution, wave deformation takes place over the nonlinear time scale, τ_{NSW}, obtained by balancing the orders of magnitude of the nonlinear terms and time derivatives in (4.4) and (4.5). The magnitude of η and that of the spatial variations are given by $\eta \sim a_0$ and $\partial_x \sim 1/\lambda_0$ respectively. Furthermore, for relatively small amplitudes, the magnitude of the horizontal fluid velocity is dictated by the linear phase speed $\tilde{u} \sim \omega_0 \eta \sim a_0\sqrt{g/d}$. The slow nonlinear time scale, τ_{NSW}, is then obtained from the balance $\tilde{u}_t \sim \tilde{u}\tilde{u}_x$, or, equivalently, $\eta_t \sim \tilde{u}\eta_x$, which yields

$$\tau_{NSW} = \frac{\lambda_0}{a_0}\sqrt{\frac{d}{g}}. \tag{4.6}$$

The breakdown of dispersion-free dynamics as given by the hyperbolic system (4.4) and (4.5) occurs at a critical time, t_s, which represents the appearance of shocks in the wave profile (i.e. the time when pure shallow-water dynamics would produce an infinite slope). For moderate wave amplitudes (approximately 70 % of the total depth), the critical time t_s also corresponds to the formation of undular bores (for higher amplitudes a hydraulic jump forms, see, e.g. Peregrine (1966)). This process has been examined most recently by Madsen, Fuhrman & Schäffer (2008) and Tissier *et al.* (2011); however, the question remains regarding whether the evolution preserves the same time scale after the generation of fast undulations as modulation theory assumes under fully nonlinear dynamics.

In order to address this point, we carry out numerical simulations of the full Euler equations, in which we monitor the variation of the maximum wave elevation in time. Results are shown in figure 5 for different choices of λ_0/d and two values of a_0/d. In these plots, time units are scaled by τ_{NSW} (operation denoted by a $\star$ superscript) and the nominal value of $t_s^\star$ is defined as the time corresponding to the change of slope from the run at the largest value of λ_0/d considered. This combination of scaling and shifting produces a clean collapse of the curves for large wavelengths. Most notably, such a collapse is observed for $t^\star > t_s^\star$, indicating that the growth of fast oscillations is driven by background shallow-water dynamics. This result supports the asymptotic description of undular bores given by modulation theory, and shows that it remains accurate also for fully nonlinear wave evolution, at least to the extent of providing the correct time scale of wave amplification. In figure 5 we further see that the maximum wave amplification occurs at $t^\star \approx 0.08 + t_s^\star$, and that after this saturation point the wave amplitude decreases gently. We can also appreciate how incomplete scale separation, i.e. moderate λ_0/d values, limits the maximum amplification attainable. We note that the analogous results shown by Wei *et al.* (1995) did not extend to a time scale sufficient to observe this second stage. Finally, by contrasting figures 5(*a*) and (*b*), we see that the growth law shows only approximate scaling with respect to the normalized wave amplitude a_0/d, as the limiting curves show minor yet notable differences. Such an incomplete scaling is to be expected due to strongly nonlinear effects. The enhancement of wave amplification by stronger nonlinearity is in line with previous analyses (Peregrine 1966; Wei *et al.* 1995).

The separation between the initial length scale λ_0 and the characteristic scale of the fast undulations is illustrated by the wave spectra reported in figure 6. The location of the first high-wavenumber spectral peak, corresponding to the scale of the fast

https://doi.org/10.1017/jfm.2014.217 Published online by Cambridge University Press

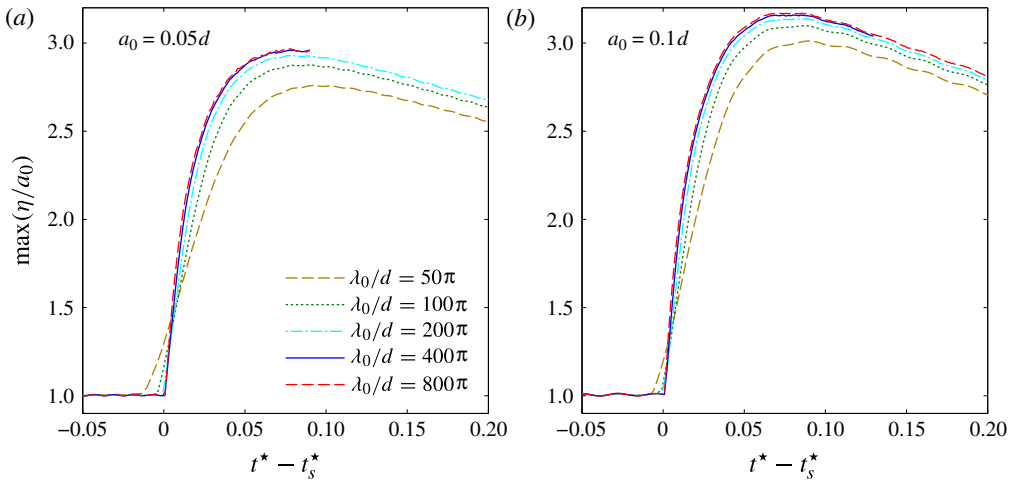


FIGURE 5. (Colour online) Normalized maximum free-surface elevation versus non-dimensional time scaled in shallow-water units and shifted by t_s, the nominal shock formation time. From full Euler simulations of developing periodic undular bores.

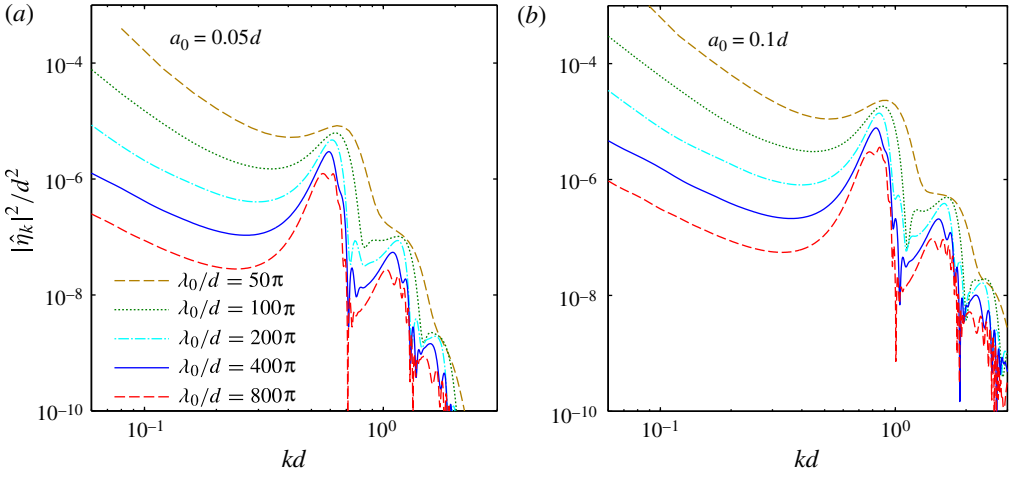


FIGURE 6. (Colour online) Instantaneous Fourier power spectrum of the surface elevation for developed periodic undular bores (from the same Euler simulations as considered in figure 5). Spectra are computed at the time of maximum wave amplification in figure 5. One should note the upshift of the first spectral peak, corresponding to the rapid dispersive waves, in (*b*) (characterized by higher wave amplitude).

undulations, does not vary with λ_0/d, whereas it shifts towards higher wavenumbers for stronger nonlinearity (as shown by contrasting (*a*) with (*b*)). This fact hints at a possible drawback in assuming that the long-time accuracy of the SGN model is improved by simply increasing λ_0/d.

All the results and considerations presented in this section provide a useful background for an understanding of the conditions leading to extreme wall runup, as will be discussed in what follows.

https://doi.org/10.1017/jfm.2014.217 Published online by Cambridge University Press

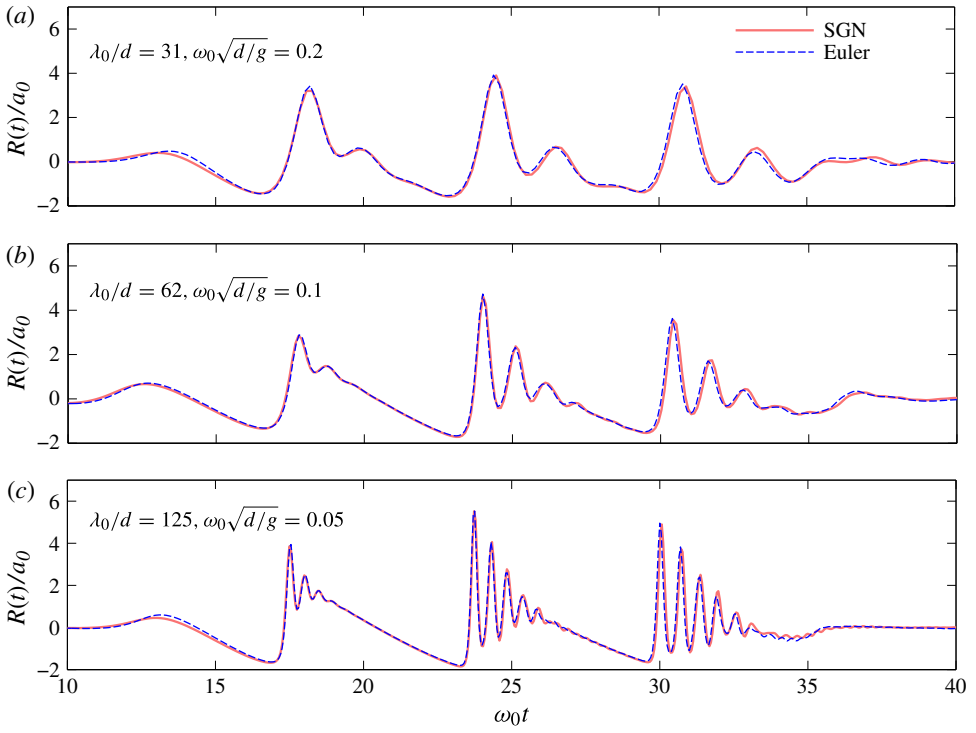


FIGURE 7. (Colour online) Wall runup history for different non-dimensional initial wavelengths, and for both Euler and SGN evolutions. Time is normalized by the linear frequency. All the runs share the same initial amplitude $a_0 = 0.05d$.

4.2. *Effect of wavelength on the runup*

In this section we focus on the effect of the non-dimensional initial wavelength λ_0/d on the wave runup, for a fixed initial wave amplitude $a_0 = 0.05d$. We observe that 5 % of the total water depth compares realistically with measurements of tsunami amplitudes within the continental shelf, as documented, for instance, by Grue *et al.* (2008). We keep the ratio L/λ_0 constant to maintain a constant proportion between the propagation distance and the wavelength, whereby we can isolate the effect of scale separation between horizontal and vertical scales. The specific choice $L = 6\lambda_0$ is made here because it realizes a critical runup condition with respect to the parameter L/λ_0, as will be shown in the next section. We span the range $30 < \lambda_0/d < 1250$, which corresponds to the frequency range $0.005 < \omega_0\sqrt{d/g} < 0.2$, and which on typical oceanic scales is associated with landslide-generated to tsunami waves.

Three examples of the wall runup temporal history for different values of λ_0/d are shown in figure 7, where computations performed with both full Euler and SGN systems are compared. The first evident feature consists of the time separation between the slow modulations imprinted by the initial condition and the fast oscillations caused by the ensuing development of undular bores. Using the time scale $\omega_0 t$, the modulation period appears to be constant, whereas the time scale of the fast oscillation shrinks with respect to the linear wave period $T_0 = 2\pi/\omega_0$. It is also apparent that the maximum runup is enhanced for longer waves. Finally, we observe that deviations between the two mathematical models are so far unnoticeable.

https://doi.org/10.1017/jfm.2014.217 Published online by Cambridge University Press

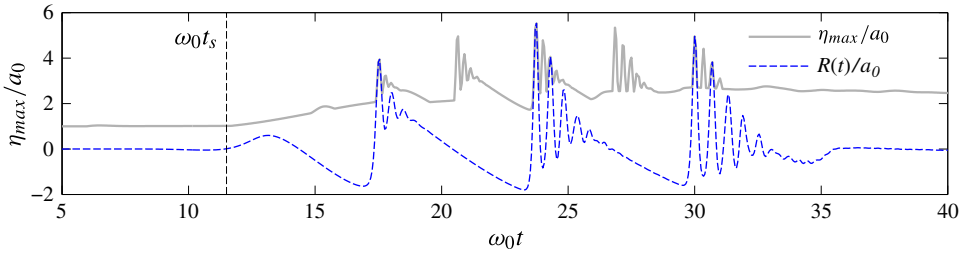


FIGURE 8. (Colour online) Comparison between the normalized wall runup (dashed line) and the normalized global maximum of the surface elevation in the entire domain (solid line), for $\omega_0 = 0.05\sqrt{g/d}$ and $a_0 = 0.05d$, from a full Euler computation. The vertical line references the incipience of fast undulations at $\omega_0 t = \omega_0 t_s$.

Wave amplification occurring prior to the wall interaction can be observed in figure 8. From this figure we can note how wave growth sets in sharply, which provides an operational definition of the shock formation time t_s analogous to the one adopted in the previous section. We note that peaks of wall runup always coincide with absolute maxima of the surface elevation in the entire domain, $\eta_{max}(t) \equiv \max_x[\eta(x, t)]$, whereas wave elevations of comparable magnitude develop inside the tank between consecutive runup cycles. These extreme events are due to the interaction between reflected and incoming waves (as visualized in figure 4).

We next consider how the maximum wave runup R_{max} over the entire time history depends on λ_0. As can be seen in figure 9, R_{max} increases monotonically with λ_0/d and tends to settle on a limiting value slightly above $6.5a_0$ for large λ_0/d. This trend can be interpreted in the light of the scaling analysis presented in § 4.1. We observe first that wave groups, as they undergo nonlinear evolution, experience an overall drift at the linear shallow-water phase speed, $c_s = \sqrt{gd}$. We can then define a conventional propagation time, i.e. the time needed by the wave group to reach the wall, as

$$\tau_P = (L - 9/4\lambda_0)/\sqrt{gd}, \tag{4.7}$$

where $L - 9/4\lambda_0$ is the initial distance from the centre of the wavepacket to the wall. Since we have set $L = 6\lambda_0$, the propagation time is proportional to λ_0/c_s across this set of simulations, and therefore proportional to the nonlinear time scale τ_{NSW} (4.6), as a_0 is constant. As τ_{NSW} is the leading time scale relevant to wave amplification throughout the entire process, as shown in § 4.1, wavefronts have the same amount of available time (on the nonlinear scale) prior to the interaction with the wall, and therefore reach the same stage of development by the time of the impact. This scaling argument, which is accurate for large λ_0/d, justifies the existence of a limiting value of R_{max}. On the other hand, the attenuation of the runup efficiency for moderate values of λ_0/d reflects the effect of moderate scale separation shown in figure 5.

As previously mentioned, the accuracy of the SGN model in capturing the evolution of undular bores is not an obvious fact *per se*, as the characteristic wavelength of the fast dispersive waves does not dilate along with λ_0/d. Figure 9 shows how the SGN model tends to slightly underestimate the runup with respect to the full Euler equations, and we observe no convergence of the long-wave model despite the increase of λ_0/d. It is further worth noting how other strongly nonlinear models applied to similar conditions produce the opposite effect, i.e. overpredict the wave elevation. This is the case for the strongly nonlinear Boussinesq model considered by Wei *et al.* (1995). In § 4.4 we shall encounter conditions in which the accuracy of the SGN model degrades more dramatically.

https://doi.org/10.1017/jfm.2014.217 Published online by Cambridge University Press

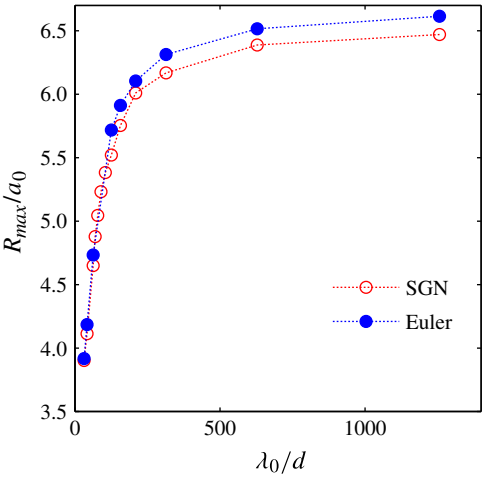


FIGURE 9. (Colour online) Normalized maximum wall runup versus non-dimensional initial wavelength, for fixed amplitude $a_0 = 0.05d$ and domain length $L = 6\lambda_0$.

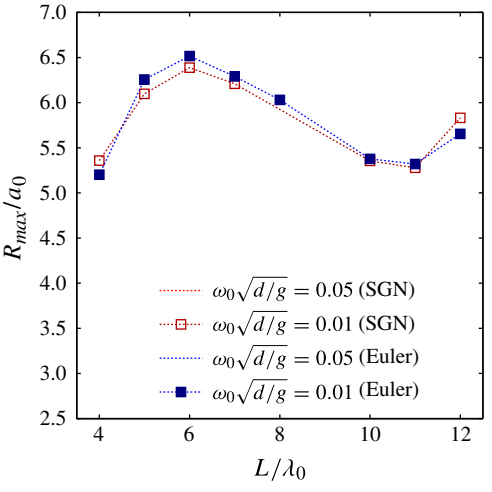


FIGURE 10. (Colour online) Normalized maximum wall runup versus non-dimensional domain size, i.e. propagation distance, for fixed amplitude $a_0 = 0.05d$.

4.3. *Effect of propagation distance on the runup*

We next analyse how the vertical runup is affected by the available propagation length before waves interact with the wall. We vary the domain size L in the range $4\lambda_0 \leqslant L \leqslant 12\lambda_0$ for fixed λ_0/d. We also report two cases, $\lambda_0/d = 125$ and $\lambda_0/d = 628$. As shown in the previous section, the first case represents an intermediate choice of λ_0, with sufficient scale separation to allow for fully developed dynamics, yet not completely assimilable to the $\lambda_0/d \to +\infty$ limit. The second case, on the contrary, represents an extreme long-wave (tsunami-like) regime.

The maximum runup obtained as a function of L/λ_0 is reported in figure 10. For moderate propagation length, wavefronts impinge on the wall before fast oscillations develop, yielding low runup values (see figure 11*a*). The wall runup then rapidly

https://doi.org/10.1017/jfm.2014.217 Published online by Cambridge University Press

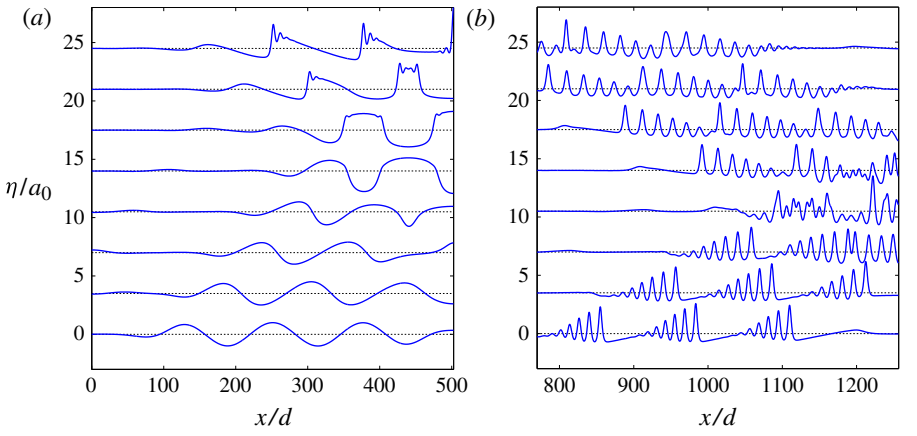


FIGURE 11. (Colour online) Runup occurring prior to undular bore development (a, $L/\lambda_0 = 4$) and after undular bore saturation, i.e. decay stage (b, $L/\lambda_0 = 10$). The snapshots show the free surface elevation obtained from full Euler simulations taken at $\Delta t = 100\sqrt{d/g}$ intervals (time increases upward and curves are progressively upshifted). The wall coincides with the right end of the x domain.

increase with L/λ_0, up to the point of maximum efficiency around $L = 6\lambda_0$, which justifies the choice of referring to such a distinguished domain length we made in the previous section. The optimal values $R_{max} \sim 5.5a_0$ and $R_{max} \sim 6.4a_0$ are found for $\lambda_0 = 125d$ and $\lambda_0 = 628d$ respectively. Indeed, as discussed in the previous section, large scale separation favours runup efficiency. The existence of an optimal condition is connected to the maximum amplification time of undular bores (shown in § 4.1). In fact, a specific domain length allows such a maximum amplification time to coincide with the propagation time τ_P, thereby leading to the maximum wall runup. As a_0/d is constant, the maxima of the two curves reported in figure 10 occur at the same L/λ_0. For higher values of L/λ_0 the runup efficiency decreases, as undular bores saturate and then decay for a long time. The contrast between the typical wave evolution at short and long propagation length is visualized in figure 11.

The last data point of the upper curve in figure 10 shows that for extremely long propagation length the runup trend can reverse. In this case, in fact, it becomes possible to observe overtaking of the trailing waves in the wake of an undular bore by the leading edge of the following one, which is another mechanism that is able to produce enhanced runup.

4.4. *Effect of nonlinearity and global runup scaling*

In this section we focus on the effect of the normalized initial amplitude a_0/d, which sets the degree of nonlinearity in the system. The highest amplitude that we consider here is probably quite unrealistic in comparison with the typical amplitude of long oceanic waves; nonetheless, it is instructive to push the comparison between the full Euler system and the SGN model up to extreme regimes. The maximum amplitude of $a_0 = 0.15$ was found to produce conditions on the verge of wave breaking; this value then represents the limit of applicability of the potential-flow formulation and consequently of our numerical model in the present conditions.

We first vary a_0 in the range $0.01d \leqslant a_0 \leqslant 0.15d$, while keeping all other parameters constant. We set $L = 6\lambda_0$ and $\omega_0\sqrt{d/g} = 0.05$. The measured runup curves are shown

https://doi.org/10.1017/jfm.2014.217 Published online by Cambridge University Press

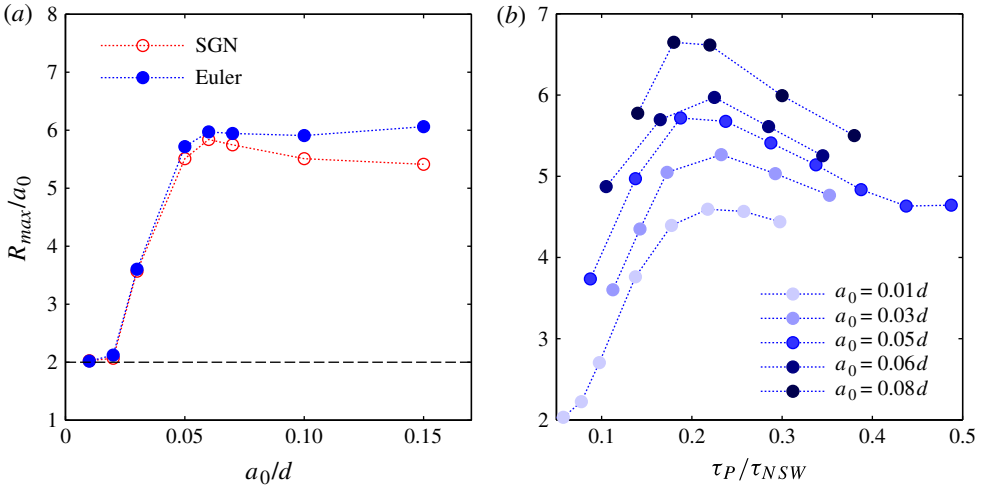


FIGURE 12. (Colour online) (*a*) Normalized maximum wall runup versus dimensionless initial amplitude, for fixed wavelength $\lambda_0 = 125d$ and domain size $L = 6\lambda_0$. The dashed line represents the linear prediction $R_{max}/a_0 = 2$. (*b*) Normalized maximum runup versus the propagation to nonlinear timescale ratio from Euler simulations, with constant $\lambda_0 = 125d$.

in figure 12(*a*). Low values of a_0/d yield the linear value $R_{max}/a_0 \approx 2$, which comes without any significant deformation of the wave profile during evolution. Clearly, nonlinearity eventually steepens the wave profile for any value of a_0/d, however small, but the corresponding nonlinear time scale τ_{NSW} dilates, deferring the onset of nonlinear effects to indefinitely long time and propagation distance. For increasing amplitude a sharp transition takes place (in the range $0.02 < a_0/d < 0.05$), where the runup behaviour changes from a linear to a fully nonlinear regime. It is interesting to note that the behaviours of the Euler and SGN systems split significantly beyond the $a_0 = 0.05d$ threshold. This fact reflects the loss of accuracy that the SGN model encounters for very high amplitudes, as also reported, for instance, by Li *et al.* (2004), who compared SGN and full Euler computations of solitary waves near the limiting amplitude.

Since the nonlinear time scale τ_{NSW} changes with a_0, we expect a corresponding variation of the maximum runup condition in terms of domain length and propagation time. In particular, the optimal domain length ($L = 6\lambda_0$ for $a_0 = 0.05d$) depends on a_0/d. We can expect, however, that the optimal condition can still be determined independently of a_0/d by plotting R_{max} as a function of the ratio τ_P/τ_{NSW} between the propagation and nonlinear time scales. In order to verify this point, we carry out a further set of runs for different values of both a_0/d and L/λ_0, as reported in figure 12(*b*). Along each individual curve τ_{NSW} is constant, whereas τ_P changes through L. These results show a good collapse of the maximum runup condition around $\tau_P/\tau_{NSW} \approx 0.22$ for any value of a_0/d, confirming that a more general criterion for the identification of extreme runup conditions in the present set-up is provided by the comparison between the propagation and nonlinear time scales.

As a conclusive observation, we can appreciate from figure 13 the effect of the acceleration of the nonlinear time scale on the runup history. By comparison between (*a*) and (*b*), and the corresponding case at $a_0 = 0.05d$ shown in figure 8, we see that higher amplitudes cause the wave groups to be more dispersed by the time they reach

https://doi.org/10.1017/jfm.2014.217 Published online by Cambridge University Press

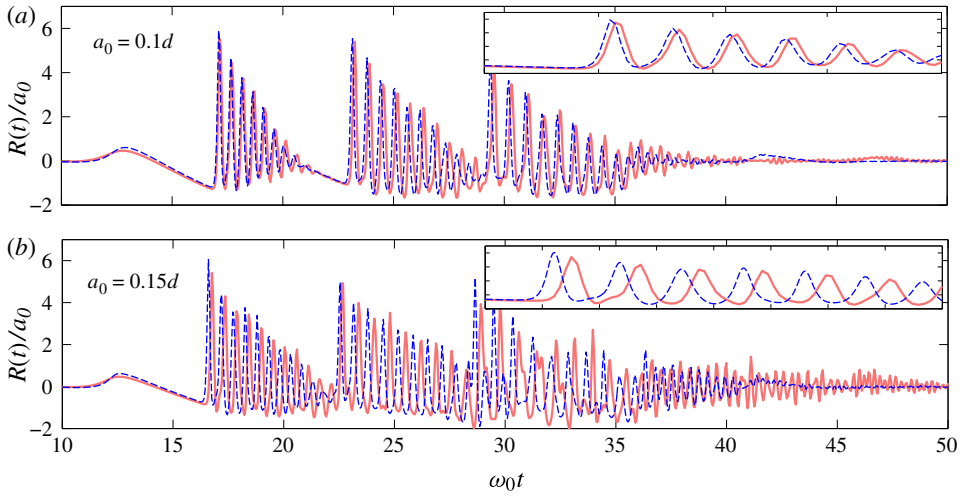


FIGURE 13. (Colour online) Runup at the wall for two initial wave amplitudes $a_0 = 0.1d$ (*a*) and $a_0 = 0.15d$ (*b*) at fixed $\omega_0 = 0.05\sqrt{g/d}$ and for both SGN (solid line) and Euler (dashed line) temporal evolution. The insets show a magnification of the time range $16 < \omega_0 t < 20$.

the wall. This is a manifestation of the nonlinear dispersion of modulated cnoidal waves. The SGN system is found to produce a slight phase lag and an enhanced shedding of trailing waves for $a_0 = 0.15d$ with respect to the full Euler evolution.

5. Conclusions

We have investigated numerically the vertical runup that can be achieved by long-wave groups propagating toward a vertical wall, extending in several directions a previous study by Carbone *et al.* (2013). The main focus of this work is on identifying the conditions leading to extreme near-wall wave amplification inside a parametric space that spans a wide range of spatial and temporal scales. This study therefore constitutes an attempt to define possible worst-case scenarios which can be useful, for example, to improve upon the notion of a design wave in coastal engineering. We have documented the existence of maximum runup amplifications up to $R_{max} \approx 6.5a_0$, corresponding, for a realistic value of $a_0 = 0.05d$, to $\approx 33\,\%$ of the water depth d (and, for the extreme case of $a_0 = 0.015d$, to even the entire water depth), whose typical dimensional magnitude lies in the range $d \approx 10$–50 m.

The disintegration of long waves in nonlinearly dispersive wavepackets (i.e. undular bores) represents the key element for the generation of extreme runups. In fact, runup efficiency depends on the evolution time available to the incoming waves prior to the interaction with the wall. We have examined (in § 4.1) the time scale that characterizes the wave height growth in undular bores within an evolving non-homogeneous background, finding that the nonlinear-dispersive dynamics following the bore formation is characterized by the nonlinear shallow-water time scale τ_{NSW} despite the breakdown of shallow-water theory. This result is in line with the assumptions of nonlinear modulation theory, and shows that this theory provides a robust description also in the case of full Euler evolution. The use of full Euler simulations therefore adds significant value to the theoretical description provided by El *et al.* (2006),

https://doi.org/10.1017/jfm.2014.217 Published online by Cambridge University Press

based on the asymptotic analysis of an SGN reduced wave model (it is not clear, for instance, that modulation theory holds accurately during the onset of the undular bore, when waves are certainly not assimilable to a slowly modulated wave train, or for intermediate scale separations).

The results that followed (§§ 4.2–4.4) confirmed the connection between the dynamics of undular bores and wall runup. In fact, the relevance of the time scale τ_{NSW} is reflected by the specific dependence of the highest runup on the physical parameters defining the initialization of the problem (λ_0/d, L/λ_0, a_0/d). In particular, we have documented that an optimal ratio between the nonlinear and propagation time scales, $\tau_P/\tau_{NSW} \approx 0.22$, is a robust indicator of the optimal runup condition, regardless of the specific combination of parameters producing such a value. We stress that such a criterion is effective for sufficiently large scale separation and for sufficiently strong nonlinearity.

In order to assess the performance of a reduced wave model often employed in the study of tsunami and landslide-generated waves, we also have compared results obtained from the SGN system with those obtained from the full Euler dynamics. We have found that, in general, this model tends to underestimate wave runup; even though its accuracy is satisfactory for moderate wave amplitudes, it degrades progressively in moving toward highly nonlinear regimes.

The set-up considered in this study, albeit rather idealized, was able to provide valuable insight regarding the potential of long waves in generating critical runup conditions. A natural extension of this work would consider the presence of variable bathymetry, which can be handled by an extended conformal-mapping approach (Viotti, Dutykh & Dias 2014). Another avenue that will be considered in forthcoming work consists of the analysis of the pressure loads exerted on the wall by near-wall extreme waves.

Acknowledgements

The authors are grateful to D. Dutykh for providing the Serre–Green–Naghdi spectral solver used in this study and for many fruitful discussions. This research was supported by the European Research Council under the research project ERC-2011-AdG 290562-MULTIWAVE and Science Foundation Ireland under grant number SFI/12/ERC/E2227.

REFERENCES

ANTUONO, M. & BROCCHINI, M. 2007 The boundary value problem for the nonlinear shallow water equations. *Stud. Appl. Maths* **119** (1), 73–93.

ANTUONO, M., LIAPIDEVSKII, V. & BROCCHINI, M. 2009 Dispersive nonlinear shallow water equations. *Stud. Appl. Maths* **122** (1), 1–28.

BARTHÉLEMY, E. 2004 Nonlinear shallow water theories for coastal waves. *Surv. Geophys.* **25**, 315–337.

BONA, J. L., PRITCHARD, W. G. & SCOTT, L. R. 1980 Solitary-wave interaction. *Phys. Fluids* **23**, 438–441.

BYATT-SMITH, J. G. B. 1988 The reflection of a solitary wave by a vertical wall. *J. Fluid Mech.* **197**, 503–521.

CAMFIELD, F. E. & STREET, R. L. 1968 Paper 6380. *J. Waterways Harbors Div. ASCE* **95**, WW1, 1.

CARBONE, F., DUTYKH, D., DUDLEY, J. M. & DIAS, F. 2013 Extreme wave run-up on a vertical cliff. *Geophys. Res. Lett.* **40**, 3138–3143.

CHAMBAREL, J., KHARIF, C. & TOUBOUL, J. 2009 Head-on collision of two solitary waves and residual falling jet formation. *Nonlinear Process. Geophys.* **16**, 111–122.

https://doi.org/10.1017/jfm.2014.217 Published online by Cambridge University Press

CHAN, R. K. C. & STREET, R. L. 1970 A computer study of finite-amplitude water waves. *J. Comput. Phys.* **6**, 68–94.

CHOI, W. & CAMASSA, R. 1999 Exact evolution equations for surface waves. *J. Engng Mech.* **125** (7), 756–760.

CIENFUEGOS, R., BARTHÉLEMY, E. & BONNETON, P. 2007 A fourth-order compact finite volume scheme for fully nonlinear and weakly dispersive Boussinesq-type equations. Part II: boundary conditions and validation. *Intl J. Numer. Meth. Fluids* **53**, 1423–1455.

CIENFUEGOS, R., BARTHÉLEMY, E. & BONNETON, P. 2010 Wave-breaking model for Boussinesq-type equations including roller effects in the mass conservation equation. *ASCE J. Waterway Port Coastal Ocean Engng* **136**, 10–26.

COOKER, M. J., WEIDMAN, P. D. & BALE, D. S. 1997 Refection of a high-amplitude solitary wave at a vertical wall. *J. Fluid Mech.* **342**, 141–158.

CRAIG, W., GUYENNE, P., HAMMACK, J., HENDERSON, D. & SULEM, C. 2006 Solitary water wave interactions. *Phys. Fluids* **18** (5), 057106.

DIAS, F. & MILEWSKI, P. 2010 On the fully-nonlinear shallow-water generalized Serre equations. *Phys. Lett.* A **374** (8), 1049–1053.

DUTYKH, D., CLAMOND, D., MILEWSKI, P. & MITSOTAKIS, D. 2013 Finite volume and pseudo-spectral scheme for the fully nonlinear 1D Serre equations. *Eur. J. Appl. Maths* **24**, 761–787.

EL, G. A., GRIMSHAW, R. H. J. & SMYTH, N. F. 2006 Unsteady undular bores in fully nonlinear shallow-water theory. *Phys. Fluids* **18**, 027104.

FENTON, J. D. & RIENECKER, M. M. 1982 A Fourier method for solving nonlinear water-wave problems: application to solitary-wave interactions. *J. Fluid Mech.* **118**, 411–443.

FRITZ, H. M., KONGKO, W., MOORE, A., MCADOO, B., GOFF, J., HARBITZ, C., USLU, B., KALLIGERIS, N., SUTEJA, D., KALSUM, K., TITOV, V., GUSMAN, A., LATIEF, H., SANTOSO, E., SUJOKO, S., DJULKARNAEN, D., SUNENDAR, H. & SYNOLAKIS, C. 2007 Extreme runup from the 17 July 2006 Java tsunami. *Geophys. Res. Lett.* **34** (12), L12602.

FRITZ, H. M., PETROFF, C. M., CATALÁN, P. A., CIENFUEGOS, R., WINCKLER, P., KALLIGERIS, N., WEISS, R., BARRIENTOS, S. E., MENESES, G., VALDERAS-BERMEJO, C., EBELING, C., PAPADOPOULOS, A., CONTRERAS, M., ALMAR, R., DOMINGUEZ, J. C. & SYNOLAKIS, C. E. 2011 Field survey of the 27 February 2010 Chile tsunamis. *Pure Appl. Geophys.* **168**, 1989–2010.

FRITZ, H. M., PHILLIPS, D. A., OKAYASU, A., SHIMOZONO, T., LIU, H., MOHAMMED, F., SKANAVIS, V., SYNOLAKIS, C. E. & TAKAHASHI, T. 2012 The 2011 Japan tsunami current velocity measurements from survivor videos at Kesennuma Bay using LiDAR. *Geophys. Res. Lett.* **39**, L00G23.

GODA, Y. 2010 *Random Seas and Design of Maritime Structures*, Advanced Series on Ocean Engineering, vol. 33. World Scientific.

GREEN, A. E., LAWS, N. & NAGHDI, P. M. 1974 On the theory of water waves. *Proc. R. Soc. Lond.* A **338**, 43–55.

GREEN, A. E. & NAGHDI, P. M. 1976 A derivation of equations for wave propagation in water of variable depth. *J. Fluid Mech.* **78**, 237–246.

GRUE, J., PELINOVSKY, E. N., FRUCTUS, D., TALIPOVA, T. & KHARIF, C. 2008 Formation of undular bores and solitary waves in the strait of Malacca caused by the 26 December Indian Ocean tsunami. *J. Geophys. Res.* **113**, C05008.

LANNES, D. & BONNETON, P. 2009 Derivation of asymptotic two-dimensional time-dependent equations for surface water wave propagation. *Phys. Fluids* **21**, 016601.

LI, Y. A., HYMAN, J. M. & CHOI, W. 2004 A numerical study of the exact evolution equations for surface waves in water of finite depth. *Stud. Appl. Maths* **113**, 303–324.

MADSEN, A., FUHRMAN, D. R. & SCHÄFFER, H. A. 2008 On the solitary wave paradigm for tsunamis. *J. Geophys. Res.* **113**, C12012.

MADSEN, A. & SCHÄFFER, H. A. 2010 Analytical solutions for tsunami runup on a plane beach, single waves, N-waves and transient waves. *J. Fluid Mech.* **645**, 27–57.

MAXWORTHY, T. 1976 Experiments on collisions between solitary waves. *J. Fluid Mech.* **76**, 177–185.

https://doi.org/10.1017/jfm.2014.217 Published online by Cambridge University Press

MORI, N., TAKAHASHI, T., YASUDA, T. & YANAGISAWA, H. 2011 Survey of 2011 Tohoku earthquake tsunami inundation and run-up. *Geophys. Res. Lett.* **38**, L00G14.

NIKOLKINA, I. & DIDENKULOVA, I. 2011 Rogue waves in 2006–2010. *Nat. Hazards Earth Syst. Sci.* **11**, 2913–2924.

O'BRIEN, L., DUDLEY, J. M. & DIAS, F. 2013 Extreme wave events in Ireland: 14,680 BP–2012. *Nat. Hazards Earth Syst. Sci.* **13**, 625–648.

PATTERSON, G. S. & ORSZAG, A. 1971 Spectral calculations of isotropic turbulence: efficient removal of aliasing interactions. *Phys. Fluids* **14**, 2538–2541.

PELINOVSKY, E., TROSHINA, E., GOLINKO, V., OSIPENKO, N. & PETRUKHIN, N. 1999 Runup of tsunamis on a vertical wall in a basin of complex topography. *Phys. Chem. Earth* B **24** (5), 431–436.

PEREGRINE, D. H. 1966 Calculations of the development of an undual bore. *J. Fluid Mech.* **25**, 321–330.

SAINFLOU, M. 1928 Essai sur les digues maritimes verticales. *Ann. Ponts Chaussées* **98** (11), 5–48.

SERRE, F. 1953 Contribution à l'étude des écoulements permanents et variables dans les canaux. *La Houille Blanche* **8**, 374–872.

SU, C. H. & MIRIE, R. M. 1980 On head-on collisions between two solitary waves. *J. Fluid Mech.* **98**, 509–525.

TEMPERVILLE, A. M. 1979 Interaction of solitary waves in shallow water theory. *Arch. Mech.* **31**, 177–184.

TEMPERVILLE, A. M., SEABRA-SANTOS, F. J. & RENOUARD, D. P. 1987 Numerical and experimental study of the transformation of a solitary wave over a shelf or isolated obstacle. *J. Fluid Mech.* **176**, 117–134.

TISSIER, M., BONNETON, P., MARCHE, F., CHAZEL, F. & LANNES, D. 2011 Nearshore dynamics of tsunami-like undular bores using a fully nonlinear Boussinesq model. *J. Coast. Res.* **64**, 603–607.

VIOTTI, C., DUTYKH, D. & DIAS, F. 2014 The conformal-mapping method for surface gravity waves in the presence of variable bathymetry and mean current. *IUTAM Procedia* **11**, 110–118.

WEI, G., KIRBY, J. T., GRILLI, S. T. & SUBRAMANYA, R. 1995 A fully nonlinear Boussinesq model for surface waves. Part 1. Highly nonlinear unsteady waves. *J. Fluid Mech.* **294**, 71–92.

WHITHAM, G. B. 1974 *Linear and Nonlinear Waves*. Wiley Intersicence.

ZABUSKY, N. J. & KRUSKAL, M. D. 1965 Interaction of solitons in a collisionless plasma and the recurrence of initial states. *Phys. Rev. Lett.* **15**, 240–243.

ZHAO, X., LIU, H. & WANG, B. 2013 The evolvement of tsunami waves on the continental shelves with gentle slope in the China Seas. *Theor. Appl. Mech. Lett.* **3**, 032005.

ZHELEZNYAK, M. I. & PELINOVSKY, E. N. 1985 Physical and mathematical models of the tsunami climbing a beach. In *Tsunami Climbing A Beach* (ed. E. N. Pelinovsky), pp. 8–34. Applied Physics Institute Press.

https://doi.org/10.1017/jfm.2014.217 Published online by Cambridge University Press